Periodica Polytechnica
Electrical Engineering
and Computer Science

59(4), pp. 160-174, 2015
DOI: 10.3311/PPee.8507

RESEARCH ARTICLE

Hybrid Controller for Variable Speed Wind Energy Conversion System with Slip Energy Recovery Using Matrix Converter Topology

Zakaria Kara[1*], Kamel Barra[1]

Received 17 August 2015; accepted after revision 10 November 2015

Abstract

This paper presents an improved control method of variable speed Wind Energy Conversion System (WECS). The power conversion chain uses Doubly Fed Induction Generator (DFIG) supplied via Matrix Converter (MC) to ensure reliability and good energy conversion management. The proposed hybrid control method combines the merits of Sliding Mode Control (SMC) in term of robustness and high dynamic response in transients to those of Proportional Integral (PI) regulators in term of stability in steady state for constant references. The designed method uses a Fuzzy Logic Supervisor (FLS) that can switches between the two modes according to desired performance. The proposed hybrid controller is applied as a Maximum Power Point Tracker (MPPT) for two wind speed profiles, the first changes abruptly, and here we had take into account the low frequency component of the wind speed model, and the second profile take the complete wind speed model (low and high frequency components). The purpose of using two wind profile is to depict the advantages and disadvantageous of each control mode. The proposed control method provides best efficiency of the conversion chain especially for medium and high power generation systems, also, very attractive results in term of reference tracking and oscillations around Optimal Power Points (OPP) are achieved providing quick and smooth energy conversion. In addition, a unified power factor and low harmonic distortion are also achieved in the grid side.

Keywords

Wind energy conversion system, Doubly fed induction generator, Proportional Integral controller, Matrix Converter, Sliding Mode Control, Fuzzy Logic supervisor, hybrid control

[1] Electrical Engineering and Automatic Laboratory,
Department of Control Electrical Engineering ,
Faculty of Sciences and Applied Sciences,
Larbi Ben M'hidi University of Oum Elbouaghi Algeria 04543,

[*] Corresponding author, e-mail: zakkka@yahoo.fr

1 Introduction

Nowadays, wind energy conversion has acquired a mature technology and provides a clean and inexhaustible source of energy for maintaining the continuously growing energy needs of humanity.

Wind Energy Conversion System (WECS) can be classified according to speed control and power control ability [1,2]. The speed-control criterion leads to two types of WECS: fixed-speed and variable-speed wind turbines. Variable speed wind energy conversion system is the most popular used one, because it allows a maximum power extraction over a large range of wind speeds. These WECSs use generally Doubly Fed Induction Generator (DFIG) due to its flexibility (DFIG can either inject or absorb power from the grid). The stator windings are directly connected to the grid phases providing electric power with constant voltage and frequency, while the rotor windings are connected to back to back voltage source converters (two cascaded converters connected with a direct current DC link). The Rotor Side Converter (RSC) controls the active and reactive power of the generator, while the Grid Side Converter (GSC) controls the DC link voltage and ensures operation of high power factors. As the rotor speed is fluctuating, the electric power of the rotor is reversible depending on whether the machine operates in either sub-synchronous mode or super-synchronous mode. Other advantages of DFIG machines can be cited, such as the adaptability of the power factor, better efficiency, ability to control the reactive power without capacitive support, significant reduction of the power converters size and cost since the size of the converter is related to the speed variation range, typically around +/- 30% of the synchronous speed. Note that the main advantage of the WECS based DFIG machine is the perfect decoupling between active and reactive power control by controlling rotor currents [1,3,4].

During the two last decades, several control strategies for WECSs based DFIG have been reported in specialist literature starting from the basic idea that control does significantly improve all aspects of WECSs. The most widely used technique is Field Oriented Control (FOC) [4-6] where rotor currents are decomposed into direct component that controls the

torque (the stator active power) and a quadrature component that commands the rotor flux (stator reactive power) and they are regulated separately with linear PI regulators. The power control block diagram of the DFIG incorporates, generally, a cascaded structure with four PIs regulators, two PIs in the outer loops for stator active and reactive powers, and two PIs in the inner rotor currents loops. An additional MPPT controller for speed tracking is added. Simplified structures have been then proposed by eliminating sometimes inner currents loops and sometimes the outer power loops but at least the control block contains three PIs controllers [4-6].

The maximum energy capture available in the wind generator can be achieved if the turbine rotor operates on the Optimal Regime Characteristic (ORC). This regime can be obtained by tracking some target variables: the optimal rotational speed, depending proportionally on the wind speed, and the optimal rotor power [1].

In this way, the standard PI control is widely used in WECS, owing its popularity to some key features such as its simple design procedure, easy to implement, it requires little feedback information, and especially for its best tracking performance in steady state [1,5-7].

As it is well known that wind speed in WECS is very fluctuating and changes abruptly due to external atmospheric conditions, the external wind speed loop needs to be controlled with robust and fast controllers such as sliding mode controller (SMC).

In this paper, we investigate by numerical simulation the role played by the maximum power point tracking (MPPT) controller in a variable speed WECS to control the power conversion. To reduce the cost of the conversion chain, the standard converter topology that uses two back to back converters is replaced by a matrix converter (MC) topology ensuring operation at large power factor. Therefore, the MC is connected to the grid phases throw an input filter (Lf , Rf , Cf) to avoid overvoltages generation and to eliminate high- frequency harmonics in grid currents.

The global control scheme of the studied system is given in Fig. 1. The MPPT controller is used to track closely the maximum power point tracker of the wind turbine (turbine rotor works closely on the optimal regime characteristic ORC), then two PIs controllers are used to control separately the active and reactive power of the DFIG. The MC modulation technique is space vector modulation (SVM) well adequate for such application due to its low harmonic distortion and its constancy switching frequency. Note that one of the benefits of the present work is that both stator and MC converter are connected to the grid via a filter designed to avoid overvoltages and current harmonics.

The performance of the maximum power point tracking stage are simulated and given for three kinds of controllers, standard PI controller, sliding mode controller (SMC) and hybrid PI-SMC controller based fuzzy supervisor. The hybrid PI-SMC based fuzzy supervisor is synthesized in order to keep

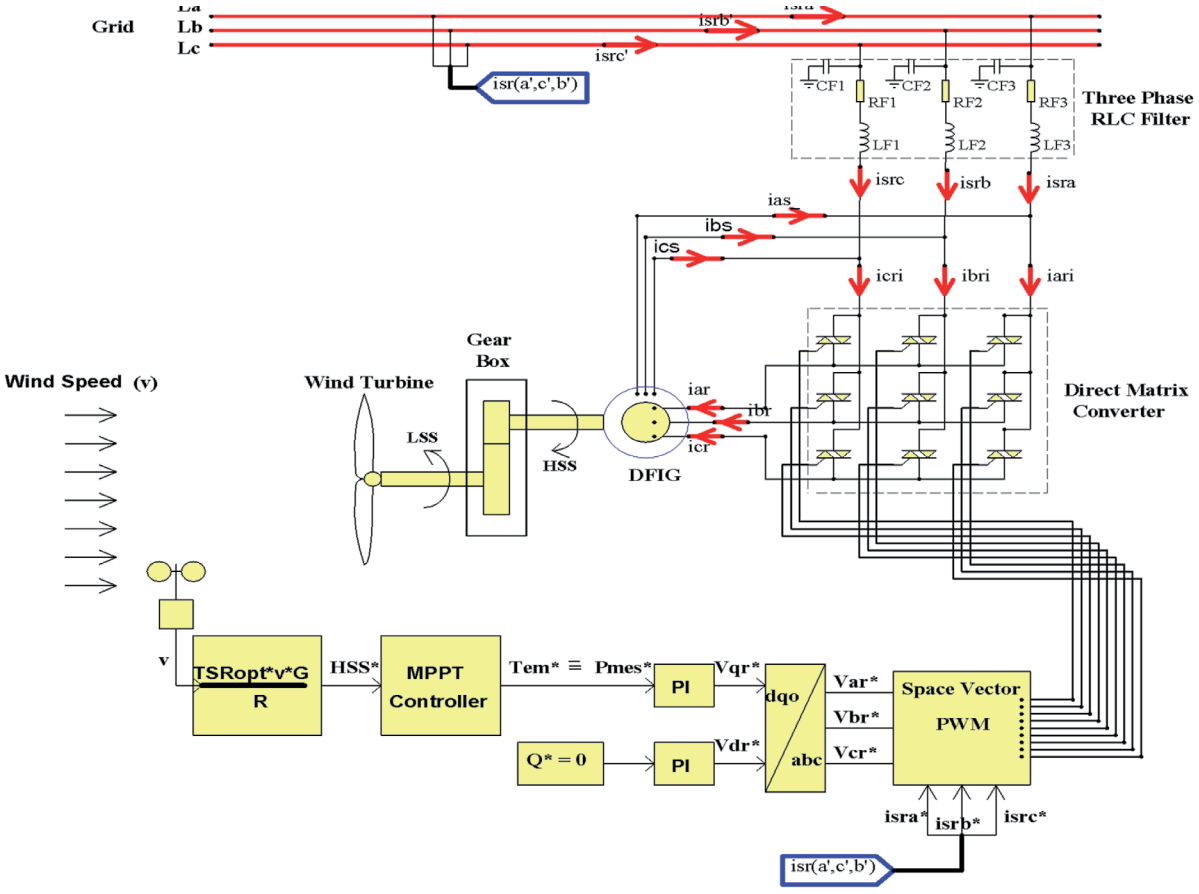

Fig. 1 Global control scheme

the SMC robustness, the high dynamic response in transients and to eliminating the torque ripples (mechanical stress) due to chattering phenomenon in steady state.

2 Modelling of the studied system

2.1 Wind speed model

Wind dynamics result from combining meteorological conditions with particular features of a given site. Wind speed is modelled in the literature as a non-stationary random process, yielded by superposing two components [1]:

$$v(t) = v_s(t) + v_t(t) \tag{1}$$

$v_s(t)$ is the low-frequency component (describing long term, low-frequency variations) and $v_t(t)$ is the turbulence component (corresponding to fast, high frequency variations). Two profile of wind speed are depicted in Fig. 2 the first one is for 5 s, only the low frequency component wind speed is used. Whereas the second take the two component for 10 s.

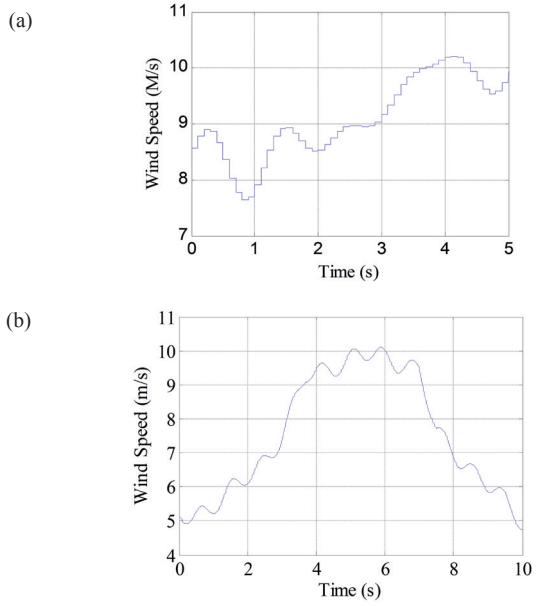

Fig. 2 First Profile of the wind speed v(t)

2.2 Wind turbine characteristics

Several variable-speed WECS configurations are being widely used in literature. The configuration studied in the present paper is a fixed pitch horizontal axis wind turbines (HAWT) having a power coefficient (aerodynamic efficiency), Cp depending on the tip speed ratio (TSR) (i.e., the ratio between the blades' peripheral speed and the wind speed: λ=Ω.R/ v) and having a maximum for λopt for a well- determined value.

The power characteristics of the wind turbine have a maximum for each wind speed. All these maxima form the so-called optimal regimes characteristics (ORC). The availible power on the the turbine shaft is [1,5]:

$$P_m = \frac{1}{2} C_p(\lambda) \cdot \rho \cdot \pi R^2 \cdot v^3 \tag{2}$$

The power coefficient Cp is then given by [5]:

$$C_p(\lambda,\beta) = C_1\left(\frac{C_2}{\lambda_i} - C_3\beta - C_4\beta^{C_5} - C_6\right)\cdot \exp\left(\frac{-C_7}{\lambda_i}\right) \tag{3}$$

$$\begin{cases} \dfrac{1}{\lambda_i} = \dfrac{1}{\lambda + C_8\beta} - \dfrac{C_9}{\beta^3 + 1} \\ \lambda = \dfrac{R\Omega}{v} \end{cases} \tag{4}$$

Figure 3 gives a 3D plot of the mechanical power captured by the wind turbine versus wind speed and high speed shaft whereas Fig. 4 depicts a 3D plot of aerodynamic efficiency Cp versus tip speed ratio λ for different values of the pitch angle β.

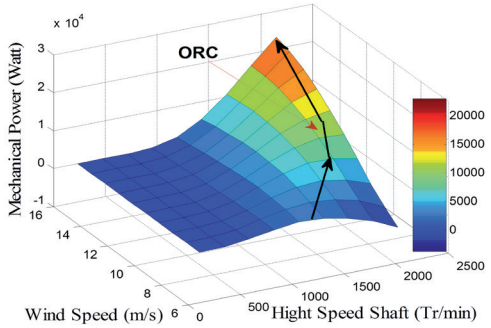

Fig. 3 Captured power versus wind speed and high speed shaft.

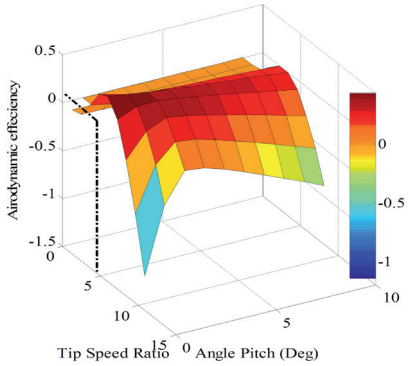

Fig. 4 Aerodynamic efficiency versus tip speed ratio and pitch angle

2.3 DFIG Model

The equations that describe doubly fed induction generator (DFIG) in a d-q reference frame, are identical to those of a squirrel cage induction generator; the only exception is that the rotor winding is not short-circuited. Here, we assume balanced voltages and non-ground connection points. The stator and rotor voltages are given by the following equations [4,6]:

$$\begin{cases} V_{ds} = R_s i_{ds} + \dfrac{d\psi_{ds}}{dt} - \omega_s \psi_{qs} \\ V_{qs} = R_s i_{qs} + \dfrac{d\psi_{qs}}{dt} + \omega_s \psi_{ds} \\ V_{dr} = R_r i_{dr} + \dfrac{d\psi_{dr}}{dt} - \omega_{sl} \psi_{qr} \\ V_{qr} = R_r i_{qr} + \dfrac{d\psi_{qr}}{dt} + \omega_{sl} \psi_{dr} \end{cases} \tag{5}$$

The electromagnetic torque is expressed as:

$$T_{em} = p\left(\psi_{ds} i_{qs} - \psi_{qs} i_{ds}\right) \tag{6}$$

where V_{ds}, V_{qs}, i_{ds}, i_{qs}, ψ_{ds}, ψ_{qs}, V_{dr}, V_{qr}, i_{dr}, i_{qr}, ψ_{dr}, ψ_{qr} are voltage components, current components and flux components of stator and rotor, respectively. The flux components are given by:

$$\begin{cases} \psi_{ds} = L_s i_{ds} + M i_{dr} \\ \psi_{qs} = L_s i_{qs} + M i_{qr} \end{cases} \qquad \begin{cases} \psi_{dr} = L_r i_{dr} + M i_{ds} \\ \psi_{qr} = L_r i_{qr} + M i_{qs} \end{cases} \tag{7}$$

In order to obtain a decoupled control of stator active-reactive powers, the DFIG model requires all quantities to be expressed under stator flux orientation concept, and assuming that the stator resistance is small when compared to the stator reactance for medium and high power size machine, the stator flux can be computed as [1,4,6]:

$$\begin{cases} \psi_{ds} \approx \psi_s \approx \dfrac{V_s}{\omega_s} \\ \psi_{qs} = 0 \end{cases} \tag{8}$$

After some manipulations, we can get from (5), (7) and (8) the stator current expressions by:

$$\begin{cases} i_{ds} = \dfrac{\psi_s}{L_s} - \dfrac{M}{L_s} i_{dr} \\ i_{qs} = -\dfrac{M}{L_s} i_{qr} \end{cases} \tag{9}$$

The stator active-reactive powers expressions are given by:

$$\begin{cases} P_s = V_{ds} i_{ds} + V_{qs} i_{qs} = -V_s \dfrac{M}{L_s} i_{qr} \\ Q_s = V_{qs} i_{ds} - V_{ds} i_{qs} = \dfrac{V_s^2}{\omega_s L_s} - \dfrac{V_s M}{L_s} i_{dr} \end{cases} \tag{10}$$

Relations (10) means that the resulting system binds proportionally the stator active power to rotor q-axis current component and the stator reactive power to the rotor d-axis current component.

The expression for the electromagnetic torque becomes:

$$T_{em} = -p \frac{M}{L_s} i_{qr} \psi_{ds} = \frac{p}{\omega_s} \left(-V_s \frac{M}{L_s} i_{qr} \right) = \frac{p}{\omega_s} P \tag{11}$$

The rotor voltage expressions are then simplified as:

$$\begin{cases} V_{dr} = R_r\, i_{dr} + \sigma L_r \dfrac{di_{dr}}{dt} - g\omega_s \sigma L_r i_{qr} \\ V_{qr} = R_r\, i_{qr} + \sigma L_r \dfrac{di_{qr}}{dt} + g\omega_s \sigma L_r i_{dr} + g\dfrac{MV_s}{L_s} \end{cases} \tag{12}$$

2.4 Matrix Converter Model

Matrix Converter is a direct AC–AC converter that uses an array of (m x n) controlled bi-directional switches to directly connect m-phase inputs to n-phase outputs. Matrix Converters (MC) have received a considerable attention these last years because of their numerous merits on the traditional AC-DC-AC converters such as no DC-link capacitor, the bi-directional power flow control (the capability of regeneration), the sinusoidal input-output waveforms and adjustable input power factor, but the biggest drawback of this technology is the high control complexity [7-10].

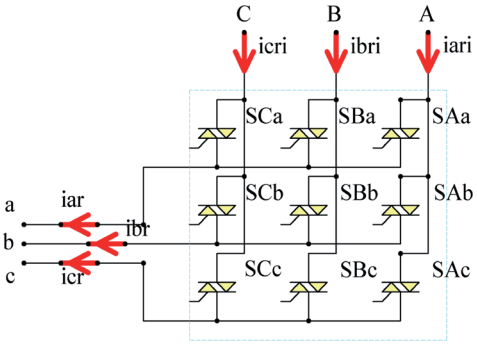

Fig. 5 Topology of matrix converter

The load current must not be interrupted abruptly, because of the inductive nature of the load that can generate an important overvoltage destroying the components. In addition, operation of the switches cannot short-circuit two input lines, because this switching state will originate short circuit currents. These two restrictions can be expressed in mathematical form by the following equation:

$$S_{Ay} + S_{By} + S_{Cy} = 1 \quad \forall \quad y \in \{a,b,c\} \tag{13}$$

Referenced to the neutral point N, the relation between the load and input voltages of the MC is expressed as:

$$\begin{bmatrix} v_{ao}(t) \\ v_{bo}(t) \\ v_{co}(t) \end{bmatrix} = \underbrace{\begin{bmatrix} S_{Aa} & S_{Ba} & S_{Ca} \\ S_{Ab} & S_{Ba} & S_{Ca} \\ S_{Ac} & S_{Ba} & S_{Ca} \end{bmatrix}}_{T} \times \begin{bmatrix} v_{ai}(t) \\ v_{bi}(t) \\ v_{ci}(t) \end{bmatrix} \tag{14}$$

where T is the instantaneous transfer matrix. The input and load voltages can be expressed as vectors as follows:

$$v_o = \begin{bmatrix} v_{ao}(t) \\ v_{bo}(t) \\ v_{co}(t) \end{bmatrix} \quad v_i = \begin{bmatrix} v_{ai}(t) \\ v_{bi}(t) \\ v_{ci}(t) \end{bmatrix} \tag{15}$$

the relation of the voltages is given by

$$v_o = T \times v_i \tag{16}$$

Then, the following equation can be obtained for rotor quantities:

$$\begin{bmatrix} i_{ari}(t) \\ i_{bri}(t) \\ i_{cri}(t) \end{bmatrix} = \underbrace{\begin{bmatrix} S_{Aa} & S_{Ab} & S_{Ac} \\ S_{Ba} & S_{Ba} & S_{Ba} \\ S_{Ca} & S_{Ca} & S_{Ca} \end{bmatrix}}_{T^T} \times \begin{bmatrix} i_{ar}(t) \\ i_{br}(t) \\ i_{cr}(t) \end{bmatrix} \tag{17}$$

Considering the current vectors

$$i_o = \begin{bmatrix} i_{ar}(t) \\ i_{br}(t) \\ i_{cr}(t) \end{bmatrix} \qquad i_i = \begin{bmatrix} i_{ari}(t) \\ i_{bri}(t) \\ i_{cri}(t) \end{bmatrix} \tag{18}$$

The equation for the current is

$$i_i = T^T \times i_o \tag{19}$$

where T^T is the transposed of matrix T.

2.5 The Indirect Space Vector Modulation

The SVM strategy, based on space vector representation becomes very popular due to its simplicity, low harmonic distortion and constancy of switching frequency. In contrast to sinusoidal PWM, SVM treats the three phase quantities as a single equation known as reference space vector given by [7,9,11]:

$$v^* = \frac{2}{3}\left(v^*_{ao}(t) + v^*_{bo}(t)\cdot e^{j2\pi/3} + v^*_{co}(t)\cdot e^{-j2\pi/3}\right) \tag{20}$$

The main idea of the indirect modulation technique is to consider the matrix converter as a two-stage transformation converter: a rectification stage to provide a constant virtual dc-link voltage Upn during the switching period by mixing the line-to-line voltages in order to produce sinusoidal distribution of the input currents, and an inverter stage to produce the three output voltages. Figure 6 shows the converter topology when the indirect modulation technique is used.

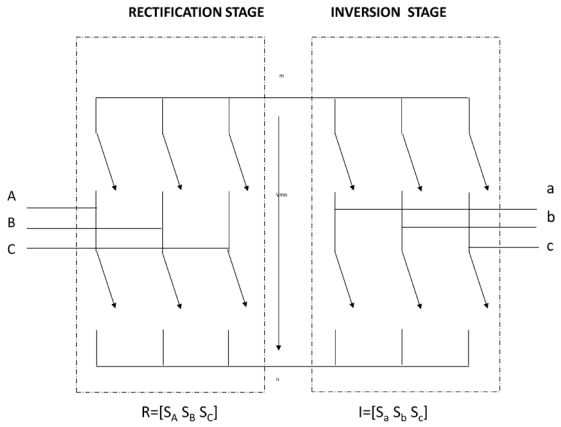

Fig. 6 The matrix converter model when an indirect modulation technique is used [7].

By multiplying the rectification stage matrix R by the inversion stage matrix I, the converter transfer matrix T is obtained:

$$T = R \cdot I$$

$$\underbrace{\begin{bmatrix} S_{Aa} & S_{Ba} & S_{Ca} \\ S_{Ab} & S_{Ba} & S_{Ca} \\ S_{Ac} & S_{Ba} & S_{Ca} \end{bmatrix}}_{T} = \begin{bmatrix} S_A \\ S_B \\ S_C \end{bmatrix} \cdot \begin{bmatrix} S_a & S_b & S_c \end{bmatrix} \tag{21}$$

This technique uses a combination of the two adjacent vectors and a zero vector to produce the reference vector. The proportion between the two adjacent vectors gives the direction and the zero-vector, and the duty cycle is determined by the magnitude of the reference vector. The input current vector that corresponds to the rectification stage of Fig. 7a and the output voltage vector that corresponds to the inversion stage of Fig. 7b are the reference vectors.

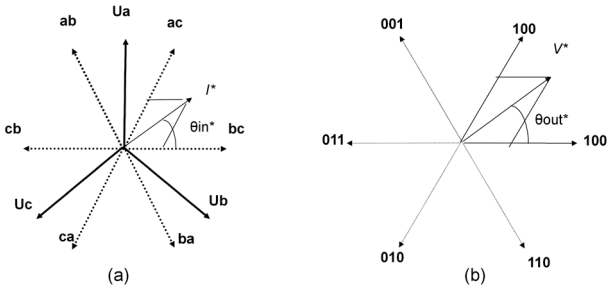

Fig. 7 Generation of the reference vectors using SVM: (a) rectification stage; (b) inversion stage [7]

In order to implement the SVM, it is necessary to determine the position of the two reference vectors. The input reference current vector I_i^* is given by the input voltage vector if an instantaneous unitary power factor is desired, or it is given by a custom strategy to compensate for unbalanced and distorted input voltage system. The output reference voltage vector V_o^* may be produced by the active and reactive powers control scheme.

When the absolute positions of the two reference vectors y_{in} and y_{out} are known, the relative positions inside the corresponding sector θ_{in}* and θ_{out}*, as well as the sectors of the reference vectors, are determined [7]:

$$\begin{aligned} \text{in}_{\text{sec}} &= \text{trunc}\left(\frac{\theta_{\text{in}}}{\pi/3}\right) \\ \text{out}_{\text{sec}} &= \text{trunc}\left(\frac{\theta_{\text{out}}}{\pi/3}\right) \end{aligned} \tag{22}$$

$$\begin{aligned} \theta^*_{\text{in}} &= \theta_{\text{in}} - \pi/3 \cdot \text{in}_{\text{sec}} \\ \theta^*_{\text{out}} &= \theta_{\text{out}} - \pi/3 \cdot \text{out}_{\text{sec}} \end{aligned} \tag{23}$$

The duty cycles of the active switching vectors are calculated for the rectification stage by using the following relations:

$$\begin{aligned} d_\gamma &= m_i \cdot \sin\left(\pi/3 - \theta^*_{\text{in}}\right) \\ d_\delta &= m_i \cdot \sin\left(\theta^*_{\text{in}}\right) \end{aligned} \tag{24}$$

and for the inversion stage by:

$$d_\alpha = m_v \cdot \sin\left(\pi/3 - \theta^*_{\text{out}}\right)$$
$$d_\beta = m_v \cdot \sin\left(\theta^*_{\text{out}}\right) \quad (25)$$

where m_i and m_v are the rectification and inversion stage modulation indexes, and $\theta_{\text{in}}{}^*$ and $\theta_{\text{out}}{}^*$ are the angles within their respective switching hexagon of the input current and output voltage reference vectors. Usually,

$$m_i = 1, m_v = \frac{\sqrt{3} \cdot v_o}{V_{mn}} \quad (26)$$

where v_o is the magnitude of the output reference voltage vector and U_{pn} is the virtual dc-link voltage. In the ideal sinusoidal and balanced input voltages, the virtual dc-link voltage remains constant:

$$V_{mn} = d_\gamma \cdot v_{\text{line}-\gamma} + d_\delta \cdot v_{\text{line}-\delta} = 0.86 \cdot \sqrt{2} \cdot v_{\text{line}} \quad (27)$$

where $v_{\text{line}-\gamma}$ and $v_{\text{line}-\delta}$ are the instantaneous values of the two line-to-line voltages to be combined in the switching period to produce the virtual dc-link and v_{line} is the magnitude of the line-to-line voltage system. Then, to obtain a correct balance of the input currents and the output voltages, the modulation pattern should be a combination of all the rectification and inversion duty-cycles ($\alpha\gamma - \alpha\delta$ - $\beta\delta - \beta\gamma$ - 0). The duty cycle of each sequence is determined as a product of the corresponding duty cycles:

$$d_{\alpha\gamma} = d_\gamma \cdot d_\alpha \;\; ; \;\; d_{\beta\delta} = d_\beta \cdot d_\delta$$
$$d_{\alpha\delta} = d_\alpha \cdot d_\delta \;\; ; \;\; d_{\beta\gamma} = d_\beta \cdot d_\gamma \quad (28)$$

The duration of the zero vectors is calculated by

$$d_0 = 1 - \left(d_{\alpha\gamma} + d_{\alpha\delta} + d_{\beta\delta} + d_{\beta\gamma}\right). \quad (29)$$

The duration of each sequence is calculated by multiplying the corresponding duty cycle by the switching period.

2.6 Input Filter Model

The input filter is very important to reduce current ripples and overvoltages with minimum installed energy on the reactive elements [7,9].

The input filter model, based on the circuit shown in Fig. 8, can be described by the following continuous-time equations [9-11]:

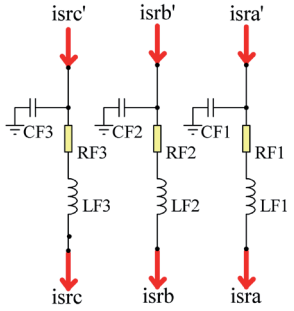

Fig. 8 Single Stage input filter

$$v_s(t) = R_f i_s(t) + L_f \frac{i_s(t)}{t} + v_i(t) \quad (30)$$

$$i_s(t) = i_i(t) + C_f \frac{v_i(t)}{t} \quad (31)$$

where L_f, R_f, C_f are the inductance, resistance and capacitance of the filter. The design of the input filter has to accomplish the following [7,9]:

- Produce an input filter with a cutoff frequency lower than the switching frequency, and higher than the fundamental frequency of the input AC source

$$\omega_n = \frac{1}{\sqrt{C_f L_f}} \quad (32)$$

$\omega_0 = 2\pi f_0$ is the resonance pulsation of the input filter.

- The input power factor should be kept maximum for a given minimum output power:

$$\frac{C_f}{P_{MCn}} = k_{\min} \cdot \tan\left(\varphi_{\min}\right) \frac{1}{3 \cdot \omega_s \cdot V_n} \quad (33)$$

where $P_{MCn} = 3 \cdot V_n$. In is the rated input active power (considering a close to unity power factor at full load). Vn; In are the rated input phase voltage and current of the converter; $P_{MC\text{-min}} = k_{\min}$. PMCn is the minimum power level where the displacement angle $\varphi_{\min}$ reaches its limit and $\omega_s = \omega_n = 2\pi f_n$ is the pulsation of the grid.

- Minimize the input filter volume or weight for a given reactive power, by taking into account the energy densities which are different for film capacitors than for iron chokes:

$$\frac{S_{Lf}}{S_{Cf}} = \frac{1}{[3 \cdot \omega_n \cdot Vn]} \left(\frac{P}{C_f}\right)^2 \quad (34)$$

Where S_{Lf} (choke), S_{Cf} (capacitor) are the installed VA in reactive components.

- The voltage drop in the inductor should be minimum to provide the highest voltage transfer ratio:

$$\frac{\Delta V}{V_n} = 1 - \sqrt{1 - \left(\omega_s \cdot L_f\right)^2 \left(\frac{I_n}{V_n}\right)^2} \quad (35)$$

The Bode diagram of the designed filter is plotted in Fig. 9, where the main frequency (60 Hz) is dashed in blue and the dominant frequency which is switching frequency (1.1 kHz) is in red, however cutoff frequency of the filter (1kHz) is in green color having a dumping factor of ξ=0.5.

3 Control strategy

Control of variable-speed fixed-pitch WECS in the partial load regime generally aims at regulating the power harvested from wind by modifying the electrical generator speed. For

each wind speed, there is a certain rotational speed at which the power curve of a given wind turbine has a maximum (Cp reaches its maximum value).

All these maxima compose what is known in the literature as the Optimal Regimes Characteristic, ORC [1].

To ensure an optimal regime it must manipulate the aerodynamic efficiency coefficient by regulating the speed generator in order to keep Cp(t,λ)= Cpmax=Cp(λopt) this is effectuated by injecting a speed set point derived from the relation (36) then a torque set point is generated. From the relationship between the torque and active power (11), a set point for the generated power is derived.

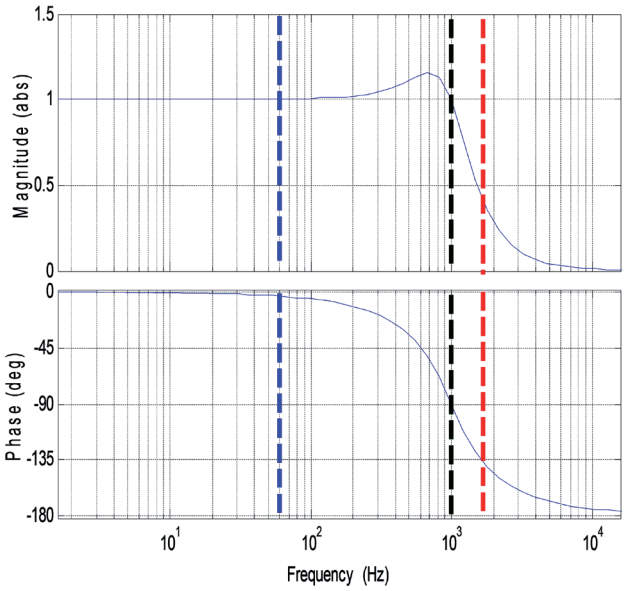

Fig. 9 Main characteristics of the designed filter

3.1 MPPT and regulator synthesis

The DFIG torque is controlled to maintain the tip speed ratio in its optimal value. The speed set point is derived from the optimal tip speed ratio as:

$$\begin{cases} \Omega = \Omega_h^* = \Omega_l^* G \\ \Omega_l^* = \dfrac{\lambda_{opt} v(t)}{R} \end{cases} \tag{36}$$

So the MPPT regulator is implement to control the turbine mechanical speed. For this purpose, two regulation modes are developed and are compared, then we have proposed a combination mode which allow us to keep advantages and to eliminate disadvantages of each one between the previous modes.

3.1.1 PI control

From system parameters (D,Jt) are positives values one can deduce the stability of our system.

The aim of the Proportional Integral regulator here is to ameliorate the system time response. The Figure 10 illustrates the control diagram using the PI regulator.

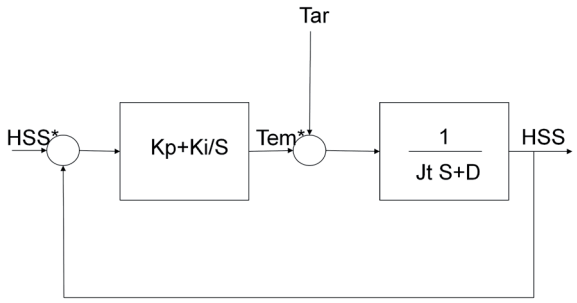

Fig. 10 PI Control scheme

The closed loop transfer function is:

$$H(S) = \frac{K_p \cdot s + K_i}{J_t \cdot s^2 + (D + K_p) \cdot s + K_i} \tag{37}$$

In order to obtain a desired first order system behaviour:

$$H(S) = \frac{1}{\tau S + 1} \tag{38}$$

the controller parameters' are expressed as :

$$K_p = \frac{J_t}{\tau} \ , \ K_i = \frac{D}{\tau} \tag{39}$$

3.1.2 The sliding mode controller

Computation of the sliding surface and of the sliding-mode control law starts from the state equations in the form [2]

$$\begin{aligned} \dot{x} &= f(x,t) + b(x,t) \cdot u \\ x &= [\Omega_h \ T_{em}] \\ f(x) &= [T_{ar}(\Omega_h, v)/J_t - T_{em} J_t - T_{em}/\tau_{ems}]^T \\ b(x,t) &= [0 \ 1/\tau_{ems}] \\ u &= T_{em}^*. \end{aligned} \tag{40}$$

The sliding mode dynamics may be imposed as equivalent to some linear ones [2].

$$\dot{\Omega} = \frac{T_{ar}(\Omega_h, v) T_{em}}{J_t} \equiv [c_1 c_2][\Omega \ T_{em}]^T \tag{41}$$

3.1.2.1 Sliding Surface

Let $s(x,u,t)$ denote the sliding surface. The condition:

$$\frac{\partial s}{\partial x} \cdot b(x,t) = 0 \tag{42}$$

existence of the equivalent control input –, require that:

$$\frac{\partial s}{\partial T_{em}} = c \neq 0 \tag{43}$$

a first form of the switching surface may be written:

$$s\left(\Omega_h, T_{em}\right) = s\left(\Omega_h\right) + c \cdot T_{em} \tag{44}$$

And when the sliding surface is reached

$$\begin{aligned} &s\left(\Omega_h, T_{em}\right) = s\left(\Omega_h\right) + c \cdot T_{em} = 0 \\ &\text{So}: s\left(\Omega_h\right) = -c \cdot T_{em} \end{aligned} \tag{45}$$

Then from Eq. (41)

$$T_{em} = \frac{1}{1 + c_2 \cdot J_t}\left(T_{ar}\left(\Omega_h, v\right) - c_1 \cdot J_t \cdot \Omega_h\right) \tag{46}$$

Here one can deduce that

$$c = 1 + c_2 \cdot J_t \tag{47}$$

Equations (46) and (45), combined with Eq. (41), gives the expression of the sliding surface [2]:

$$\begin{aligned} s\left(\Omega_h, T_{em}\right) &= c_1 \cdot J_t \cdot \Omega_h + \left(1 + c_2 \cdot J_t\right) T_{em} - T_{ar}\left(\Omega_h, v\right) \\ &= c_1 \cdot J_t \cdot \Omega_h + \left(c_2 \cdot J_t\right) T_{em} + T_{em} - T_{ar}\left(\Omega_h, v\right) \end{aligned} \tag{48}$$

$$T_{em} - T_{ar}\left(\Omega_h, v\right) = J_t \cdot \Omega_h \tag{49}$$

$$s\left(\Omega_h, T_{em}\right) = c_1 \cdot J_t \cdot \Omega_h + \left(c_2 \cdot J_t\right) T_{em} + J_t \cdot \Omega_h \tag{50}$$

3.1.2.2 Sliding-mode Control Law

Now the two components of the sliding mode control law are computed : the equivalent control input, ueq , and the onoff component, U_N.

To compute the equivalent control input the following relation is used:

$$u_{eq} = -\left[\frac{\partial s}{\partial x} b\right]^{-1} \cdot \left[\frac{\partial s}{\partial t} + \frac{\partial s}{\partial x} \cdot f\left(x, t\right)\right] \tag{51}$$

We compute part by part:

$$\begin{aligned} \left[\frac{\partial s}{\partial x} b\right]^{-1} &= \left[\left[\frac{\partial s}{\partial \Omega_h} \frac{\partial s}{\partial T_{em}}\right] \cdot \begin{bmatrix} 0 \\ 1/\tau_{ems} \end{bmatrix}\right]^{-1} \\ &= \left[\frac{1}{\tau_{ems}} \frac{\partial s}{\partial T_{em}}\right]^{-1} = \left[\frac{1 + c_2 \cdot J_t}{\tau_{ems}}\right]^{-1} \\ &= \frac{\tau_{ems}}{1 + c_2 \cdot J_t} \end{aligned} \tag{52}$$

$$\frac{\partial s}{\partial t} = 0 \tag{53}$$

$$\frac{\partial s}{\partial \Omega_h} = c_1 \cdot J_t - \frac{1}{\tau_{ems}} \cdot \frac{\partial T_{ar}}{\partial \Omega_h} \tag{54}$$

$$\begin{aligned} \frac{\partial T_{ar}}{\partial \Omega_h} &= 0.5\pi\rho R^3 v^2 \frac{\partial\left(C_P\left(\lambda\right)/\lambda\right)}{\partial \Omega_h} \\ &= Qv^2 \frac{\partial\left(C_P\left(\lambda\right)/\lambda\right)}{\partial \lambda} \frac{\partial \lambda}{\partial \Omega_h} \end{aligned} \tag{55}$$

where $Q = 0.5\pi\rho R^3$

$$\frac{\partial\left(C_P\left(\lambda\right)/\lambda\right)}{\partial \lambda} = \frac{\lambda \cdot C_p\left(\lambda\right) - C_p\left(\lambda\right)}{\lambda^2} \tag{56}$$

$$\frac{\partial \lambda}{\partial \Omega_h} = \frac{R}{G \cdot v} \Big/ \partial \Omega_h = G \cdot \partial \Omega_L \tag{57}$$

$$\frac{\partial s}{\partial \Omega_h} = c_1 \cdot J_t - \frac{Q \cdot R \cdot v}{\tau_{ems} \cdot G}\left(\frac{\lambda \cdot C_P^{\bullet}\left(\lambda\right) - C_P\left(\lambda\right)}{\lambda^2}\right) \tag{58}$$

$$\frac{\partial s}{\partial T_{em}} = 1 + c_2 \cdot J_t \tag{59}$$

By replacing each one of Eqs. (52), (57), (58) and (59) in the Eq. (51) of the equivalent control input, one obtains after some algebra:

$$\begin{aligned} u_{eq} &= T_{em} - \frac{\tau_{ems}}{1 + c_2 \cdot J_t} \cdot \\ &\left[\left(c_1 \cdot J_t - \frac{QRv}{G} \frac{\lambda \cdot C_P^{\bullet}\left(\lambda\right) - C_P\left(\lambda\right)}{\lambda^2}\right)\left(c_1 \Omega + c_2 T_{em}\right)\right] \end{aligned} \tag{60}$$

Parameter c_1 is chosen to impose the convergence speed to the sliding mode regime: $c_1 = -1/\tau_{sd}$ where the time constant $\tau_{sd} > 0$. The value of c_2 results from imposing the "target" steady state as being the Optimal operating point (OOP), corresponding to λopt :

$$\begin{aligned} &\dot{\Omega} = c_1 \Omega_{opt} + c_2 T_{opt} = 0 \\ &c_2 = -c_1 \frac{\Omega_{opt}}{T_{opt}} \end{aligned} \tag{61}$$

c_1 is the negative inverse of the time constant and c_2 is the (static) gain. One may attempt to dynamically modify c_2, using the following expression [2]:

$$c_2 = -c_1 \frac{\Omega_{opt}}{T_{opt}\left(1 + K \dfrac{\left(\Omega - \Omega_{opt}\right)}{\Omega_{opt}}\right)} \tag{62}$$

Where $K > 0$ as a tradeoff parameter.

The nonlinear control component U_N (on-off) is chosen as:

$$U_N = -A \cdot sign_\Delta(s) \qquad A > 0 \tag{63}$$

Δ: the hysteresis band.

Figure 11 to 12 illustrate a comparative show for the High Speed Shaft (HSS) (Ω) tracking for each control mode (PI & SMC). We simulate for two wind speed profiles presented in Fig. 2 in order to show the control robustness when the wind velocity changes abruptly as depicted in Fig. 2a, and for continue variation as depicted in Fig. 2b.

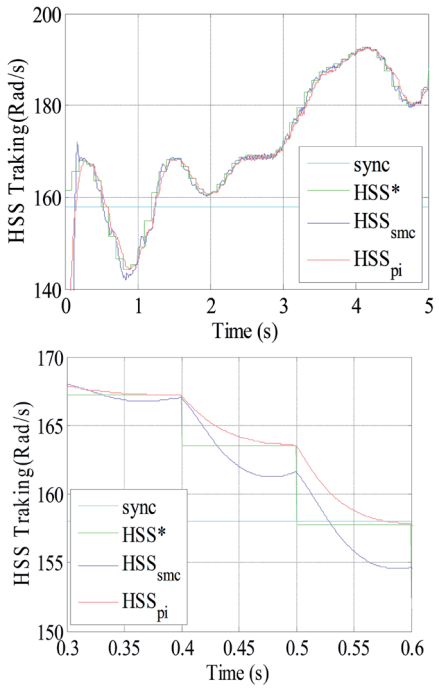

Fig. 11 High Speed Shaft (HSS) tracking for both PI and SMC controllers.

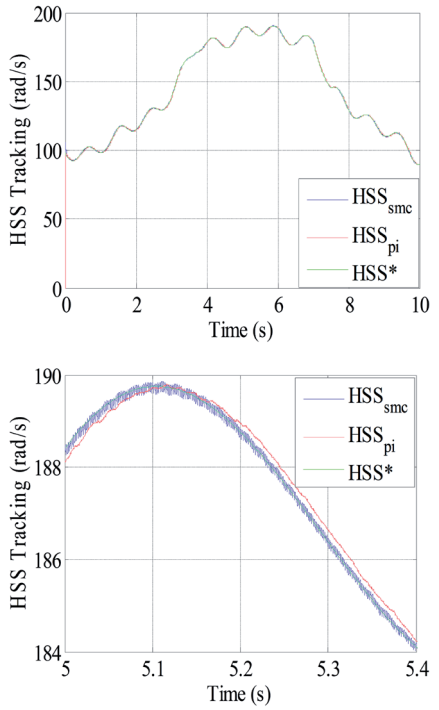

Fig. 12 Torque Tracking performance for both PI and SMC controllers

The performance of the MPPT tracking control is tested for both PI and SMC controllers for the wind speed profile of Fig. 2. One can see easily that the SMC provide high dynamic performance in transients than PI but it oscillates in steady state around its reference due to chattering phenomenon causing mechanical stress, losses in the power conversion chain, and undesirable ripples on electromagnetic torque, whereas, the PI controller gives best performance in steady state with stable profile.

3.1.3 Hybrid control

The main contribution of our work is to design a new hybrid control that combines the merits of the two precedent controllers. The hybrid control uses a fuzzy logic supervisor that switches between the two modes according to desirable performance.

The inputs of the proposed supervisor are basically the speed tracking error (e) and its variation (de). The law combining between the PI and SMC commands uses the following expression:

$$U = \delta \times U_{PI} + (1-\delta) \times U_{SMC} \tag{64}$$

Where δ is a weighting factor generated by the fuzzy supervisor. The base rules are chosen in order to get $\delta = 0$ when the system is far from the OPP; and $\delta = 1$ when the system reaches the new OPP.

Figure 13 depict (a) the speed error, (b) the error variation and (c) the weighting factor, whereas Fig. 14 illustrates the surface generated by the supervisor.

3.2 Power control

The schematic control of the studied power system is illustrated by Fig. 1; where the active power set point is derived from torque reference signal witch results from the speed tracking loop however the reactive power is settled to 0 in order to keep a unity power factor in the generated power:

$$\begin{cases} P^* = \dfrac{\omega_s}{p} T_g^* \\ Q^* = 0 \end{cases} \tag{65}$$

The both active-reactive power PI regulators are synthesized by the same manner of speed PI regulator, and the system regulated is the described one in the 12 equations set.

4 Simulation results

The numerical simulations of the proposed hybrid controller are evaluated on Matlab-Simulink hardware for the wind speed profiles depicted in Fig. 2a and 2b for both subsynchronous and super-synchronous mode.

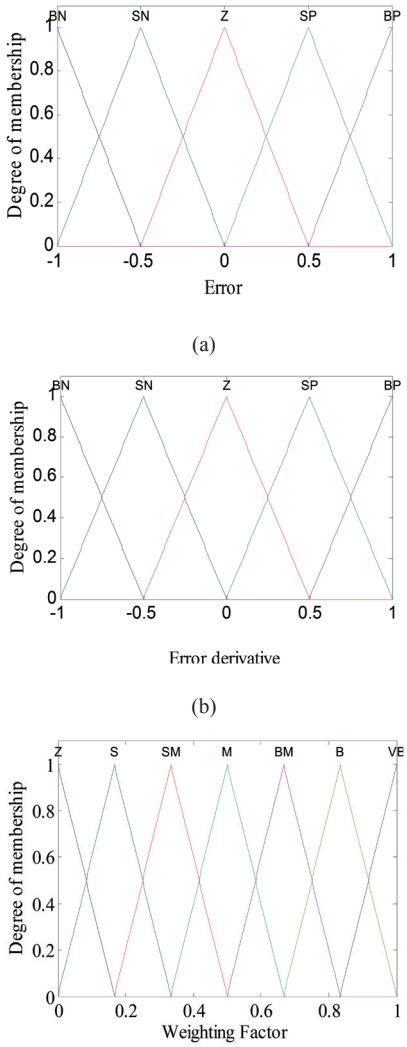

Fig. 13 (a), (b) Error fuzzification and its variation, (c) Output defuzzification.

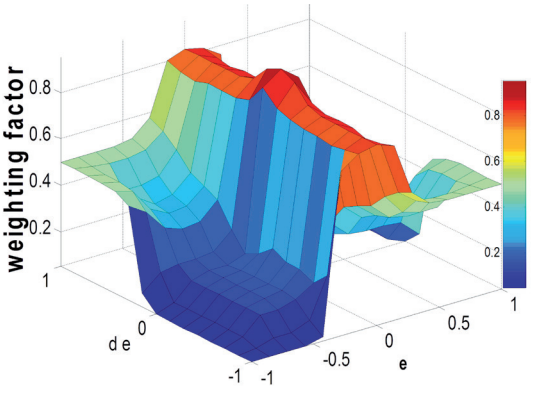

Fig. 14 The Surface evoked by the supervisor.

Figures from 15 to 18 illustrate the high speed shaft (HSS) tracking of the DFIG, the electromagnetic torque, the tip speed ratio λ and the aerodynamic efficiency Cp, when we use the profile depicted in Fig. 2a for both controllers: Hybrid, SMC and PI. It can be seen that the performance of the proposed hybrid controller are relevant compared to those of SMC and PI controllers, especially in term of fast transient duration, good robustness, stability in steady state and low torque ripples. The two most energy conversion quality indicating parameters (Cp,λ) are also depicted and they show clearly the high performance of the proposed controller since they oscillate closely around their optimal values providing high efficiency of the conversion chain. Figure 19 shows the fluctuation of the fuzzy supervisor decision (δ) that switches between the two control modes, it can be seen that when system need a quick transition from the precedent functioning point to the new one, the generated weighting factor is near to the value 1 but when it arrive to this new optimal power point the weighting factor becomes near to the value 0. The next Figures from 20 to 23 present the same variables depicted before (HSS, TSR and Cp) when the simulation based on the second wind profile, depicted in Fig. 2b this results confirm the precedent ones.

Figure 24 illustrates the stator active and reactive powers injected in the grid, where the reference reactive power is settled to 0 in order to get a unity power factor.

Figures from 25 to 28 illustrate the MC input current (i_{ari}) and the rotor current (i_{ar}), the rotor line to line voltage (vabr), the stator current (ias). On these figures one can see that all these quantities follow the variations of the wind speed profile Fig. 2a and the WECS works at unity power factor since the stator reactive power is fluctuating around 0 as can be seen in Fig. 24.

Figure 26 depicts the MC input voltage (v_{ari}) versus current (i_{ari}) for both sub-synchronous regime (case a) and hypersynchronous regime (case b), here in sub-synchronous mode, we can see that the current is in phase with the voltage; meaning that: the slip power flows from the grid to the DFIG via matrix converter, and when the machine operates in the hypersynchronous mode, the current turns in opposite phase with the voltage; meaning that: the slip power flows from the DFIG rotor to the grid via the matrix converter.

To see the role played by the designed filter, we have compared the profile of the unfiltered current (i_{sra}) and voltage (v_{sra}) before connecting with the grid (see Fig. 29a) to filtered ones (isra'), (vsra') after connecting with the grid (Fig. 29b). One can see that a significant power quality enhancement is achieved by the RLC filter proofed by the THD. In Figure 30 it is observed that the THD is reduced from THD*isra*=0.4808 (48%) for the unfiltered current to THD*isra*'=0.0482 (4.82%) for the filtered current by eliminating all harmonics that appear in the grid current specter.

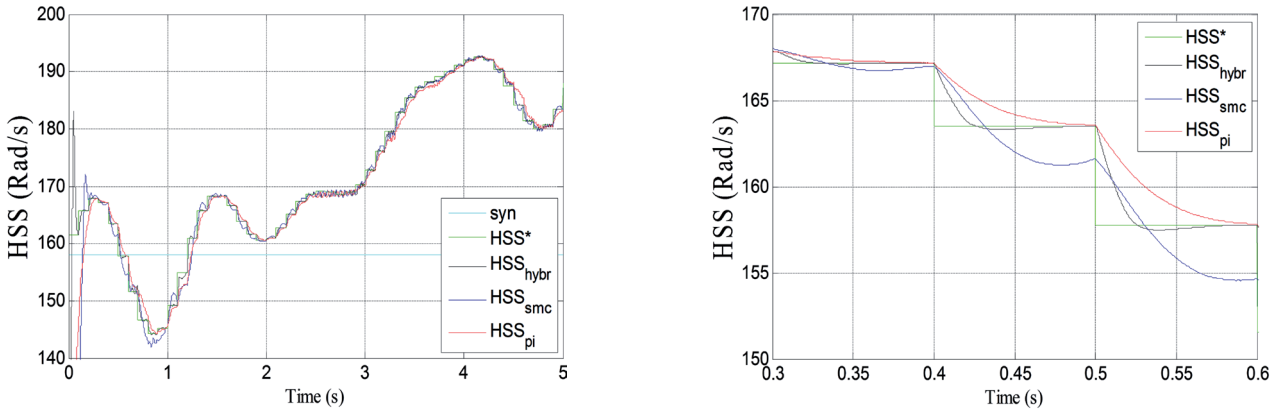

Fig. 15 High Speed Shaft Tracking (for profile in Fig. 2a)

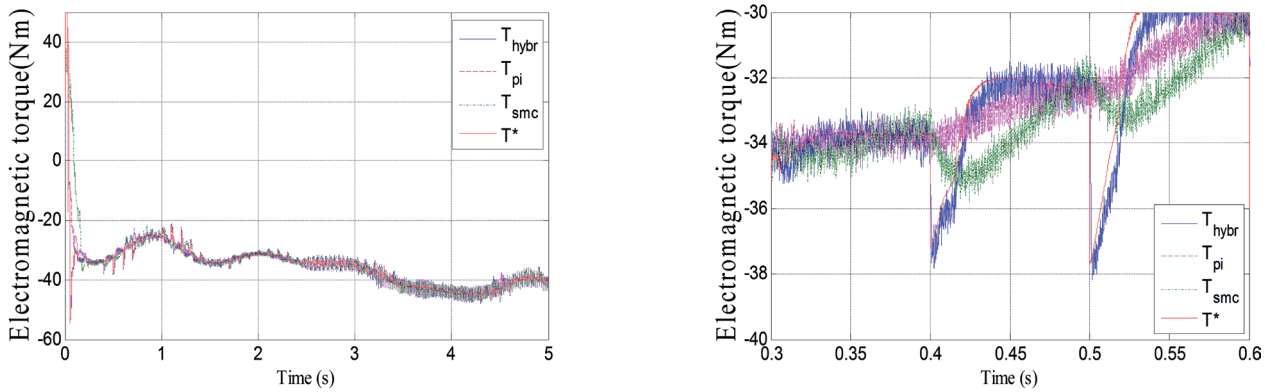

Fig. 16 Electromagnetic Torque Tracking (for profile in Fig. 2a)

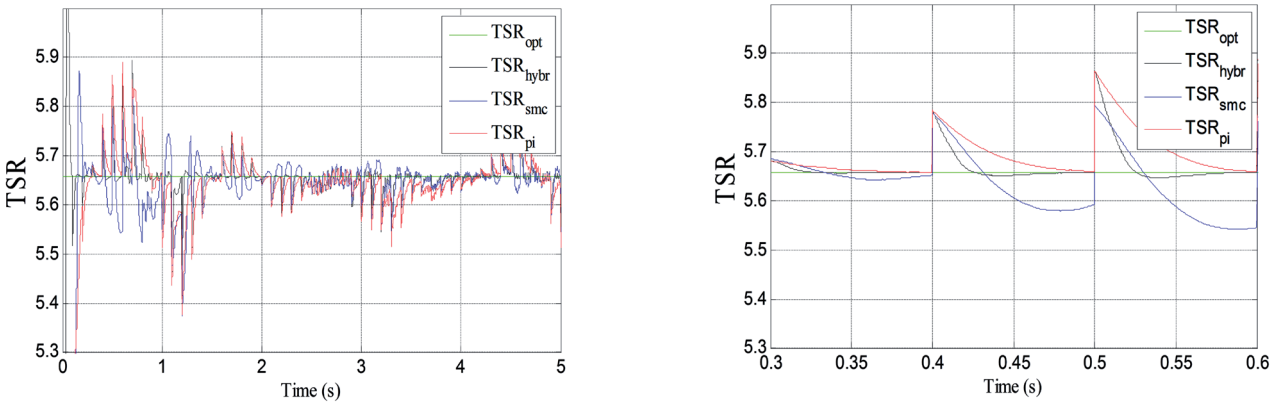

Fig. 17 Tip Speed Ratio (λ) (for profile in Fig. 2a)

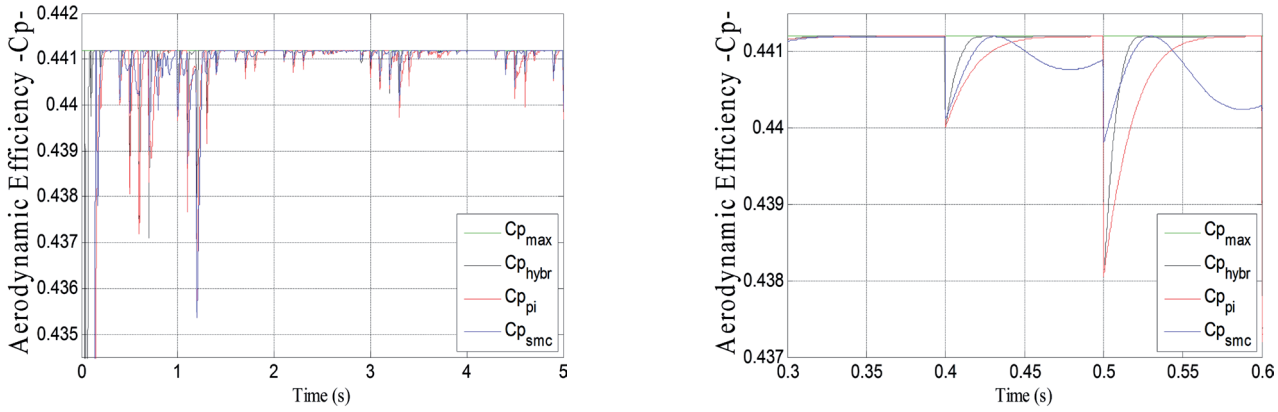

Fig. 18 Aerodynamic Efficiency (Cp) (for profile in Fig. 2a)

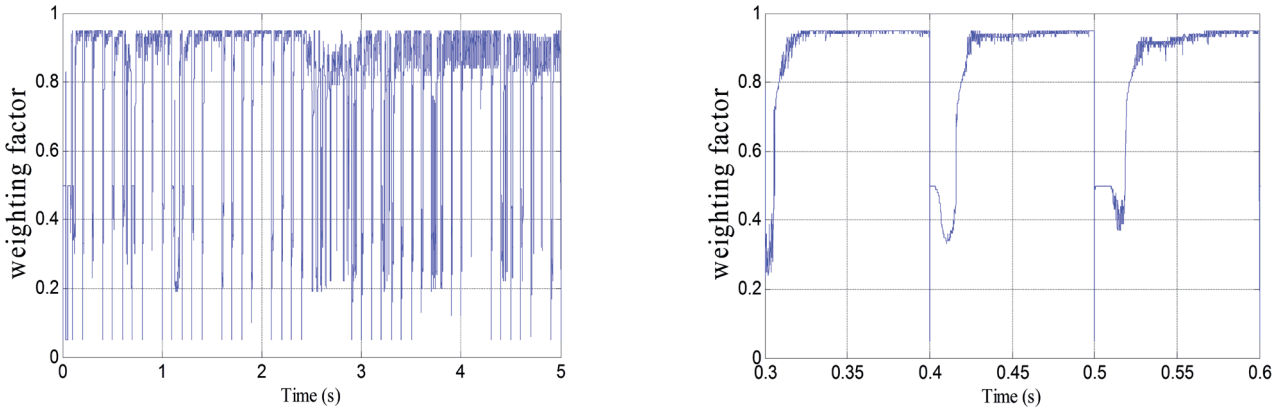

Fig. 19 Supervisor decision (δ) (for profile in Fig. 2a)

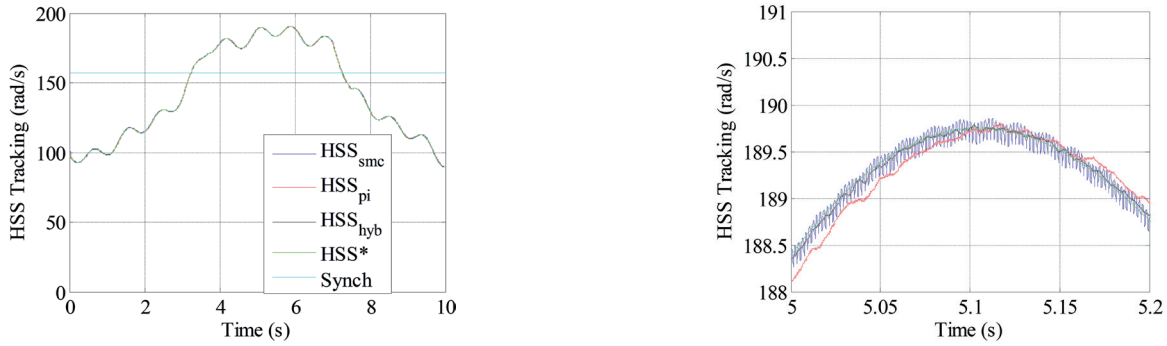

Fig. 20 High Speed Shaft Tracking (for profile in Fig. 2b)

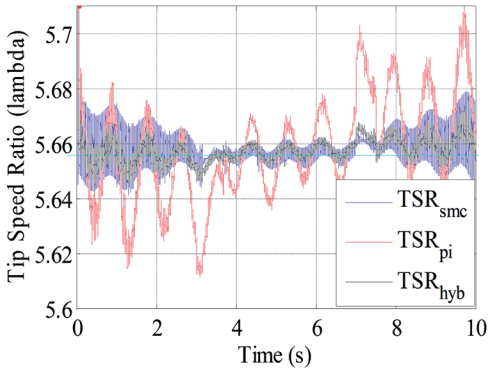

Fig. 21 Tip Speed Ratio (λ) (for profile in Fig. 2b)

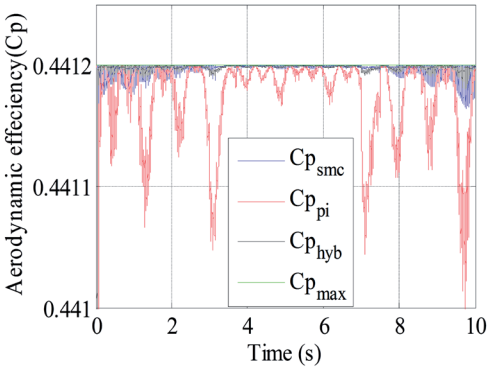

Fig. 22 Aerodynamic Efficiency (Cp) (for profile in Fig. 2b)

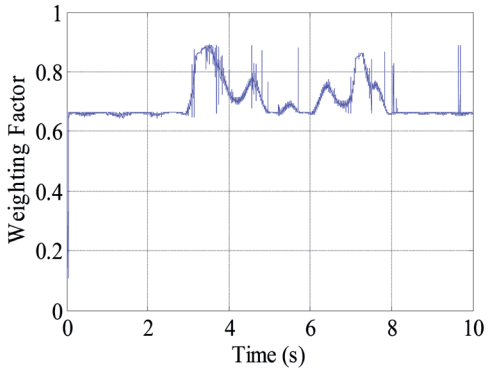

Fig. 23 Supervisor decision (δ) (for profile in Fig. 2b)

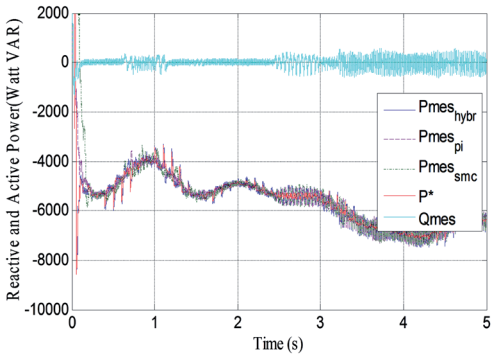

Fig. 24 Stator active and reactive powers (for profile in Fig. 2a)

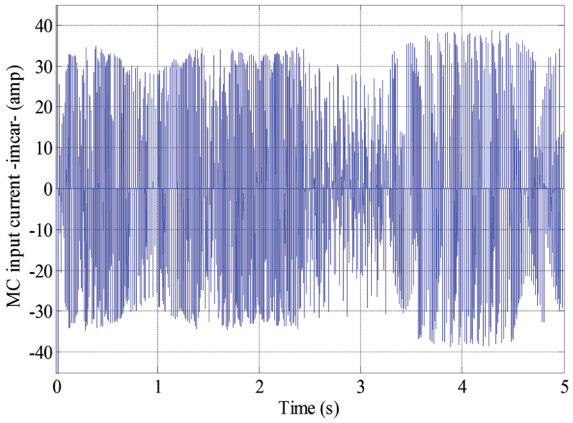

(a)

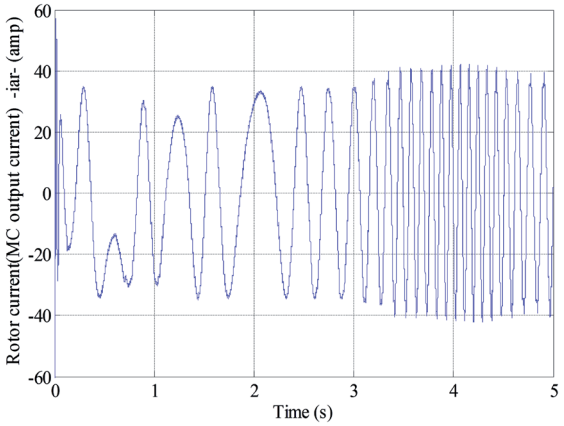

(b)

Fig. 25 (a) MC input (filter side) and (b) output (rotor side) currents

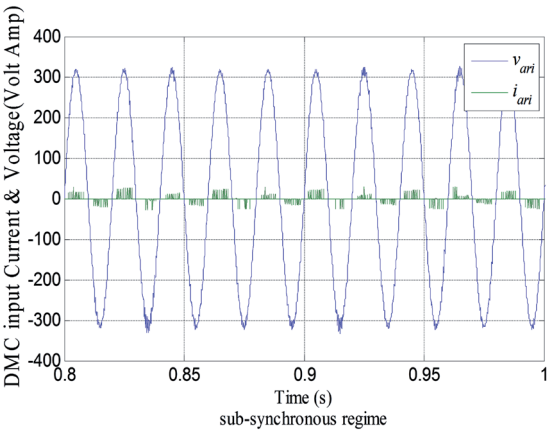

(a)

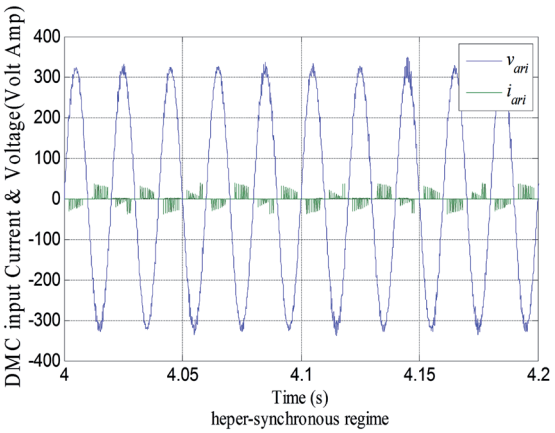

(b)

Fig. 26 MC input voltage versus current.

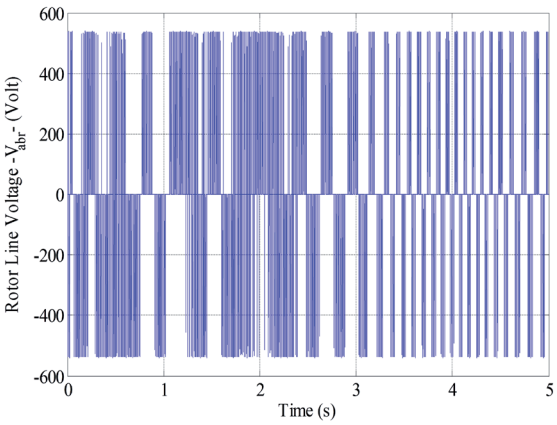

Fig. 27 Rotor line Voltage *vabr* (for profile in Fig. 2a)

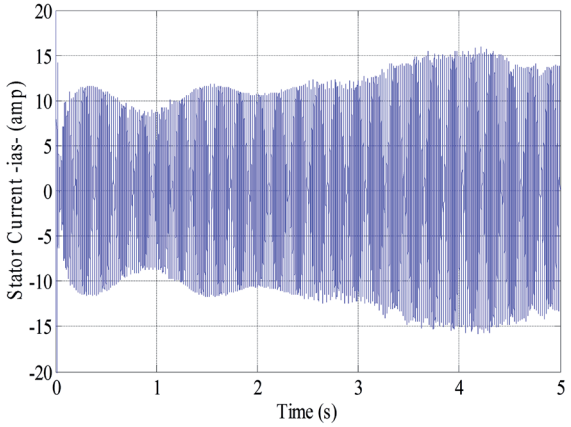

Fig. 28 Stator Current *ias* (for profile in Fig. 2a)

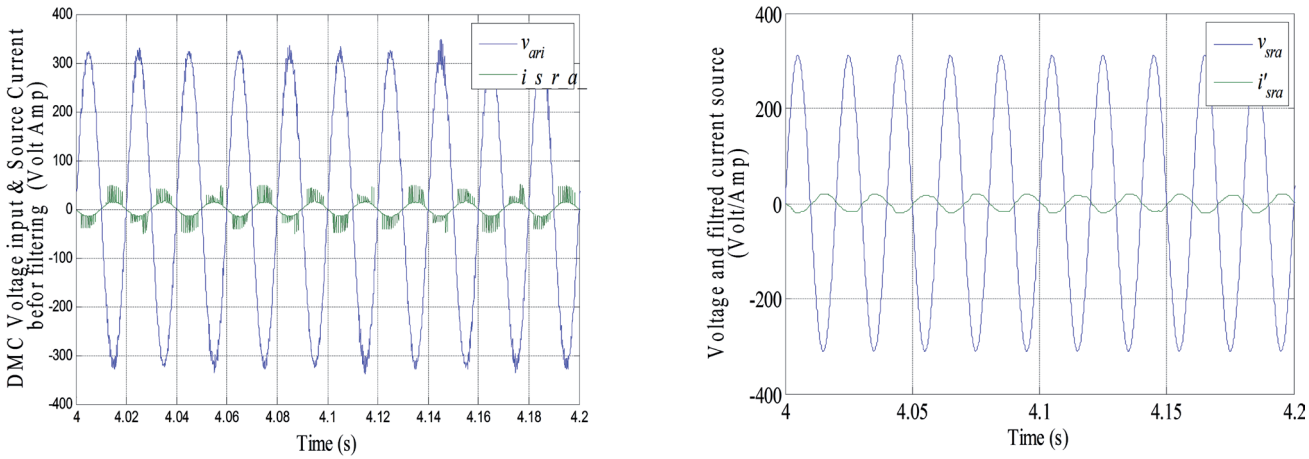

(a) (b)

Fig. 29 Current isra (a before filtering) and Current isra'(b after filtering)

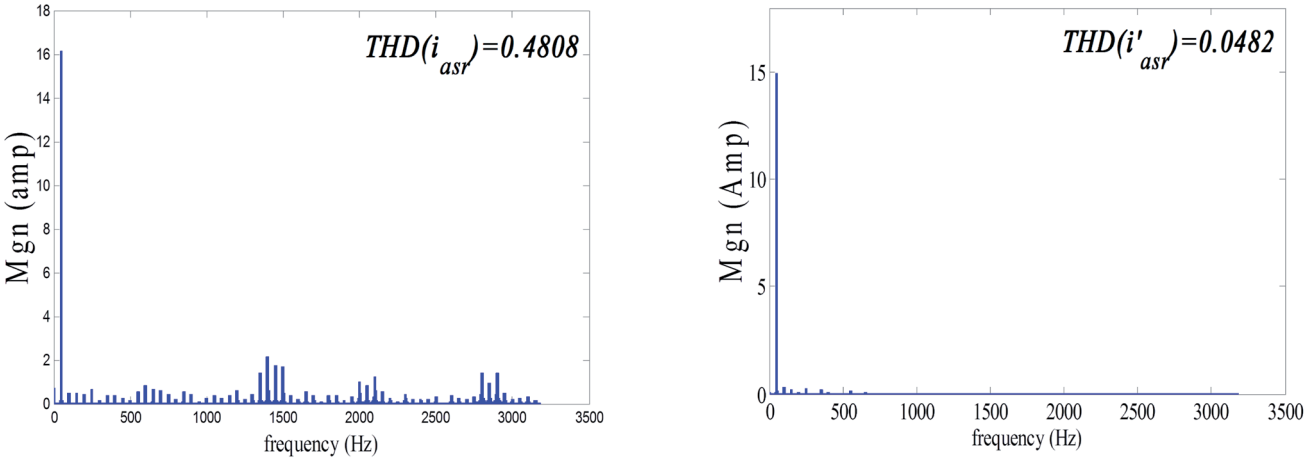

(a) (b)

Fig. 30 (a) THD of unfiltered current isra, (b)THD of filtered current isra'

5 Conclusion

In this paper, a hybrid controller for wind speed of WECS is designed to track efficiently the maximum power point. The designed controller combines the merits of sliding mode control to those of PI control to obtain an optimal regime generation. The method uses a fuzzy logic supervisor to switch between the two modes.

The studied WECS based DFIG replaces the classic back to back converters topology by a matrix converter well suited for this application. The indirect space vector modulation SVM is applied to MC. Then, RLC filter is designed to enhance power quality in the grid side by reducing the THD of grid current and voltage.

Over the different simulation results, it is observed that the performance of the WECS system are enhanced in term of fast tracking speed, low torque ripples, high efficiency, less oscillations around optimal power points and low current/voltage distortion in the grid side.

Symbols

Mechanical symbols:

v	wind speed
ρ	air density
J_t	total inertia coefficient
D	mechanical dumping factor
G	gearbox gain
R	turbine radius
C_p C_{pmax}	aerodynamic efficiency and its maxima
$C_1 \ldots C_8$	interpolation coefficients for Cp expression
β	Pitch angle of turbine blades
λ (TSR) λ_{opt}	Tip Speed Ratio and its optimal value
Ω_l; Ω_h	Low Speed Shaft (LSS) and High Speed Shaft (HSS)
T_{em}, T_{ar}	Electromagnetic and Aerodynamic torques

Electrical symbols:

Rs ; Rr	stator and rotor resistances
Ls ; Lr ; M	stator; rotor and mutual inductances

vi ; *vo*	input and output voltages of Matrix Converter(MC)
ii ; *io*	input and output currents of MC
isa ; *iari* ; *ira*	stator current, MC input current and MC output current
isra ; *i'sra*	current source before and after filtering
Pm, *P, Q*	mechanical; active and reactive power
SAa; *SAb*….*SCc*	commutation sequences
Cf; *Lf*; *Rf*	filter parameters
ωn; *ωs* ; *ξ*	cutoff and main frequencies, dumping parameter

Controller symbols:

c_1; c_2	correspond to the first order dynamics on the sliding surface and the
τ_{em}	the time constant of the Electromagnetic System
K_p, K_i, τ	Proportional and Integral parameter, constant time of PI controller
e;de;δ	error, its variation and weighting factor

References

[1] Munteanu, I., Bratcu, A. I., Cutululis, N. A., Ceanga, E. "*Optimal control of wind energy systems*." London: Springer-Verlag. p.22-31-41-47-48-75-129. 2008. URL: http://www.springer.com/us/book/9781848000797

[2] Munteanu, I., Bacha, S., Bratcu, A. I., Roye, D. "Energy-Reliability Optimization of Wind Energy Conversion Systems by Sliding Mode Control." *IEEE Transactions on Energy Conversion*. 23 (3). pp. 975-985. 2008. DOI: 10.1109/tec.2008.917102

[3] Chen, Z., Guerrero, J., Blaabjerg, F. "A review of the state of the art of power electronics for wind turbines." *IEEE Transactions on Power Electronics*. 24 (8). pp. 1859–1865. 2009. DOI: 10.1109/tpel.2009.2017082

[4] Akel, F., Ghennam, T., Berkouk, E.M., Laour, M. "An improved sensorless decoupled power control scheme of grid connected variable speed wind turbine generator." *Energy Conversion and Management Journal*. 78. pp. 584-586, 2014. DOI: 10.1016/j.enconman.2013.11.015

[5] Ackermann, T. "*Wind Power in Power Systems*." Stockholm: John Wiley & Sons Ltd. pp. 527-562-570. 2005. DOI: 10.1002/0470012684

[6] Abad, G, Miguel, J. L., Marroyo, A. R. L. "*Doubly fed induction machine*." New Jersey: John Wiley & Sons, Inc. 2011.

[7] Kazmierkowski, M. P., Krishnan, R., Blaabjerg, F. "*Control in power electronics*." Academic Press Series In Engineering. Elsevier Science. 2002. URL: https://www.elsevier.com/books/control-in-power-electronics/irwin/978-0-12-402772-5

[8] Wheeler, P. W., Zhang, H., Grant, D. A. "A theoretical and practical consideration of optimized input filter design for a low loss matrix converter." In: *Proceedings of 5th International Conference on Power Electronics and Variable-Speed Drives*. pp. 363-367. 1994. DOI: 10.1049/cp:19940992

[9] She, H., Lin, H., Wang, X., Yue, L. "Damped input filter design of matrix converter." In: I*nternational Conference on Power Electronics and Drive Systems, PEDS*. pp. 672-677. 2009. DOI: 10.1109/peds.2009.5385684

[10] Podlesak, T. F., Katsis, D. "A 150 kVA vector controlled matrix converter induction motor drive." In: *Industry Applications Conference, 39th IAS annual meeting, conference record of the 2004 IEEE*. 3. pp. 1811-1816. 2004. URL: ieeexplore.ieee.org/iel5/9338/29652/01348771.pdf

[11] Odavic, M., Sumner, M., Zanchetta, P., Clare, J. C. "A theoretical analysis of the harmonic content of PWM waveforms for multiple-frequency modulators." *IEEE Transactions on Power Electronics*. 25 (1). pp. 131-141. 2010. DOI: 10.1109/tpel.2009.2026751

Appendix

The system used for validations has the following features:

Type: fixed pitch HAWT turbine based (high speed): rated wind speed Vr = 9.5 m/s, R=3 m.

Energetic performance: maximal value of the power coefficient Cpmax =0.44 at optimal tip speed ratio λopt= 5.65.

Constant air density: ρ=1.25 Kg/m3

Electromechanical features: Jt=0.1 Kg.m2, D= 6,73.10-3 N.m.s-1

Gearbox coefficient G=10.

Generator parameters:

Rs=0,455 Ω ; Rr=0,62 Ω ; Ls=0,084 H ; Lr=0,081 H ; M= 0.078 H ; 50 Hz,

380 V, Pn=7.5 kW, Nn=1440 rpm.